metals

MDPI

Article

Corrosion Resistance of High-Entropy Alloys in Plateau Salt-Lake Environments

Shucheng Yang [1], Jiahao Liu [1], Shuwen Guo [1], Jing Zhang [1], Huaikun Zhu [1], Zhenjie Ren [1], Yanting Pan [1], Lida Che [2], Zhanfang Wu [2], Xiangyang Li [2] and Dianchun Ju [1,*]

[1] School of Metallurgy Engineering, Jiangsu University of Science and Technology, Zhangjiagang 215600, China; ggg2335946590@gmail.com (S.Y.); 15851636436@163.com (J.L.); eyucxk5932@163.com (S.G.)
[2] CISRI HIPEX Technology Co., Ltd., Haidian, Beijing 100081, China
* Correspondence: judianchun@just.edu.cn

Abstract

The corrosion behavior of high-entropy alloys under cyclic wet–dry conditions simulating the salt-lake atmosphere was investigated. The composition, morphology, and electrochemical properties of the corrosion products formed on the alloy surface after corrosion were systematically analyzed. The results show that in a chloride-containing environment with alternating temperature and humidity, the Cr-containing oxide passive film formed on the alloy surface effectively inhibits the corrosion process in the early stages. In addition, electrochemical results show that the charge transfer resistance in the $MgCl_2$ system reaches 4.96×10^5 $\Omega \cdot cm^2$ at prolonged exposure, which is significantly higher than that in the NaCl system, indicating a lower corrosion rate. However, over time, the passive film undergoes localized rupture due to chloride ion attack and stress, leading to pitting corrosion and expansion toward the substrate. This study reveals the corrosion mechanism of high-entropy alloys in high-altitude salt-lake atmospheric environments and provides crucial insights for material design and performance optimization for their engineering applications in salt-lake scenarios.

Keywords: high-entropy alloys; salt-lake atmospheric corrosion; pitting corrosion evolution; corrosion resistance

1. Introduction

As energy exploration and resource utilization extend toward increasingly extreme environments, corrosion-induced degradation of materials under complex service conditions has become a critical challenge. Plateau salt-lakes, widely distributed across the Qinghai–Tibet Plateau as well as Central Asia and South America, are characterized by high salinity, strong alkalinity, intense ultraviolet radiation, large diurnal temperature variations, and fluctuating dissolved oxygen levels [1–5]. These harsh conditions severely compromise the long-term reliability of metallic materials, as conventional engineering alloys are highly susceptible to localized corrosion, including pitting, crevice corrosion, and stress corrosion cracking. Consequently, the development and systematic evaluation of advanced corrosion-resistant materials are of great scientific and engineering importance for such environments.

In recent years, high-entropy alloys (HEAs) have attracted significant global attention as a new class of advanced materials. Composed of multiple principal elements in near-equiatomic proportions, HEAs exhibit unique physicochemical properties and

Received: 2 April 2026
Revised: 17 April 2026
Accepted: 20 April 2026
Published: 26 April 2026

have been widely investigated for compositional design, multi-functional performance (e.g., strength-ductility synergy, irradiation resistance, and corrosion resistance), and behavior under extreme conditions. Among them, the equiatomic CoCrFeMnNi alloy (Cantor alloy) is a representative model system due to its simple single-phase face-centered cubic (FCC) structure and excellent mechanical, thermal, and corrosion properties. Its chemical homogeneity and structural stability make it an ideal benchmark for understanding the fundamental mechanisms of HEAs [6,7]. The distinctive characteristics of HEAs, including high configurational entropy, lattice distortion, sluggish diffusion, and the "cocktail effect" [8–10], contribute to their enhanced environmental resistance. In particular, HEAs containing elements such as Cr, Ni, Co, and Fe can form stable passive films in various corrosive media, significantly improving resistance to localized corrosion [11–13].

Despite these advances, most studies on the corrosion behavior of HEAs have focused on single-component simulated solutions or conventional marine environments, while investigations under plateau salt-lake conditions remain limited. Such environments involve multiple coupled factors, including high salt concentration, complex ionic composition, low atmospheric pressure, and strong radiation. In particular, the synergistic effects of various ions in salt-lake brines (e.g., Cl^-, SO_4^{2-}, CO_3^{2-}, Mg^{2+}, and Li^+) on the formation, composition, and stability of passive films on HEAs are not yet fully understood. Additionally, low dissolved oxygen levels and cyclic temperature variations may further influence their electrochemical corrosion behavior. These issues warrant systematic investigation.

In this study, a CrMnFeCoNi high-entropy alloy, compositionally equivalent to the Cantor alloy, was fabricated by hot isostatic pressing (HIP) [14–16] and selected as the model material. A simulated plateau salt-lake environment containing $MgCl_2$ [17] was established to evaluate its corrosion behavior. By combining electrochemical measurements, accelerated wet–dry cyclic tests, and detailed characterization of corrosion products and surface morphology, the effects of $MgCl_2$ on passivation behavior and corrosion mechanisms were systematically analyzed. The results are expected to provide both theoretical insights and experimental guidance for the application of HEAs in plateau salt-lake and other extreme corrosive environments.

2. Materials and Methods

Table 1 lists the detailed chemical compositions of the high-entropy alloy selected as the experimental material. The alloys used in this study are equiatomic CoCrFeMnNi high-entropy alloys (Cantor alloys) prepared via hot isostatic pressing and have not undergone any subsequent processing. Plate specimens were first cut into small blocks with dimensions of 5 mm × 5 mm × 3 mm for subsequent observation of corrosion morphology and compositional analysis. The samples were then ground sequentially with SiC abrasive papers up to 1500 mesh to ensure a flat surface and to minimize the influence of initial surface defects on the experimental results. All specimens were ultrasonically cleaned in acetone to remove residual debris from the grinding process, followed by rinsing with ethanol for further surface cleaning. Finally, the samples were dried in a desiccator for 24 h to evaporate residual moisture. For electrochemical measurements, specimens were cut to the same dimensions (5 mm × 5 mm × 3 mm) and embedded in epoxy resin, leaving an exposed working surface area of 25 mm^2 for subsequent electrochemical testing.

Table 1. Chemical composition of the high-entropy alloy (wt.%).

Element	Cr	Mn	Fe	Co	Ni
Content(wt.%)	20.0	20.0	20.0	20.0	20.0

2.1. Accelerated Wet–Dry Cycling Test

To simulate the natural exposure process of the samples in the salt-lake atmosphere and accurately replicate the key characteristics of atmospheric corrosion, this study conducted accelerated wet–dry cyclic experiments using a climatic test chamber [18–22]. Considering the significant diurnal temperature variations and humidity fluctuations in salt-lake regions, the experimental parameters were specifically set to simulate these conditions. Temperature and relative humidity were key factors for replicating the day-night alternation. To investigate the effect of $MgCl_2$ on the corrosion behavior of HEAs, a control experiment using NaCl as the corrosive medium was conducted simultaneously. The experimental process is presented in Table 2.

Table 2. Experimental procedure of cyclic wet–dry immersion tests.

Step	Description	Parameters
1	Surface coating	Coated with 0.2 mol/L $MgCl_2$ (salt-lake simulation) or 0.4 mol/L NaCl (control).
2	Initial drying	40 °C ovens drying to simulate daytime evaporation
3	Wet phase	30 °C, 80% RH for 1.5 h
4	Dry phase	30 °C, 20% RH for 1 h
5	Cycling & duration	Repeated cycles to achieve total exposure of 7, 14, 21, and 28 days

The schematic diagram of this experimental procedure is shown in Figure 1. To investigate the corroded high-entropy alloy specimens, scanning electron microscopy (SEM, Coxem, Beijing, China) was employed to characterize their microstructure, and energy-dispersive X-ray spectroscopy (EDS, Oxford Instruments, Oxfordshire, UK) was used to analyze the elemental distribution. In this study, a $MgCl_2$ solution was used to simulate the salt-lake atmospheric environment because $MgCl_2$ is one of the dominant salts in many plateau salt lakes. A NaCl solution was employed as a reference chloride system commonly used in corrosion studies. The concentrations of $MgCl_2$ (0.2 mol·L^{-1}) and NaCl (0.4 mol·L^{-1}) were selected to maintain the same Cl^- concentration (0.4 mol L^{-1}) in both systems, allowing for a direct comparison of the effects of Mg^{2+} and Na^+ on the corrosion behavior of the high-entropy alloy. Although natural salt-lake brines contain multiple ions, the simplified $MgCl_2$ system can still represent chloride-dominated corrosion processes in such environments.

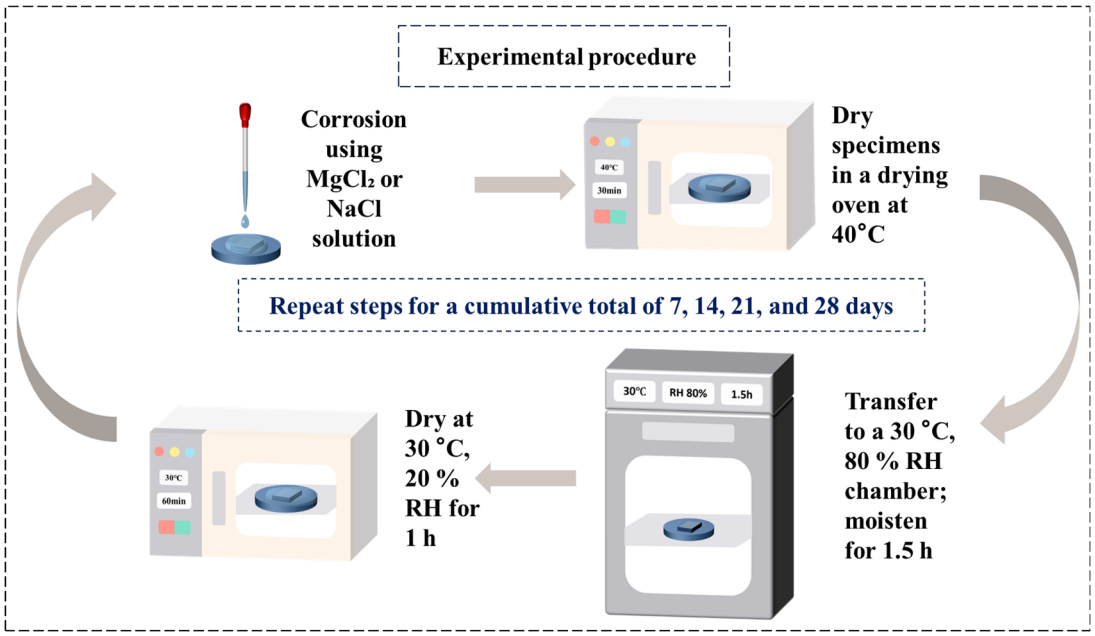

Figure 1. Flowchart of the accelerated wet–dry cyclic corrosion test simulating the salt-lake atmospheric environment.

2.2. Electrochemical Measurements

Electrochemical impedance spectroscopy (EIS) is a widely used technique for investigating metal corrosion behavior and is commonly employed for the non-destructive estimation of corrosion rates and the identification of corrosion mechanisms associated with interfacial processes. In particular, in situ EIS can provide timely information on ongoing electrochemical processes. In situ electrochemical measurements were carried out using an electrochemical workstation (CHI660E, Shanghai Chenhua Instruments Co., Ltd., Shanghai, China). All electrochemical tests were performed using a conventional three-electrode configuration, consisting of the corroding specimen as the working electrode, a platinum plate as the counter electrode, and a saturated calomel electrode (SCE) as the reference electrode. For EIS measurements, an AC perturbation with an amplitude of 10 mV was applied over a frequency range from 10^{-2} to 10^{5} Hz. The test solution was a 0.2 mol/L $MgCl_2$ solution prepared from reagent-grade chemicals and distilled water. Prior to EIS measurements, the samples were allowed to stabilize, and all measurements were conducted at room temperature. During the EIS tests, frequency sweeps were always performed from high to low frequencies, and the obtained EIS data were analyzed using ZSimpWin software 3.30. All electrochemical measurements were repeated at least three times under each condition to ensure reproducibility.

3. Results and Discussion

3.1. Morphology of Samples Under Cyclic Wet–Dry Conditions

As shown in Figure 2, the macroscopic morphologies of the corrosion products formed on the samples after exposure to a simulated salt-lake atmospheric environment for 7, 14, 21, and 28 days under $MgCl_2$ and NaCl deposition conditions are presented. Under $MgCl_2$ corrosion conditions, with increasing exposure time, the specimen surface initially exhibited a small number of isolated pitting sites with relatively uniform diameters and shallow depths. As corrosion progressed, both the depth and diameter of the pits increased simultaneously, and some pitting sites became partially covered by a thin layer of corrosion products. In contrast, the surface of the high-entropy alloy specimens subjected to NaCl deposition showed a significantly higher density of pitting sites than those corroded in $MgCl_2$

solution over the same exposure periods. From the evolution of pitting during corrosion, it is evident that the pits under NaCl conditions were uneven in size and more densely distributed. Some pits exhibited irregular elliptical shapes, accompanied by a pronounced increase in pit depth. Rough pit walls caused by the accumulation of corrosion products were observed, and the pits were filled with light-gray, loosely packed corrosion products. After 28 days of exposure, the pit depth reached its maximum, and the originally smooth and flat surface of the alloy substrate was completely destroyed, exhibiting severe pitting corrosion characteristics. These observations indicate that pitting corrosion is the dominant corrosion mode of the high-entropy alloy in both $MgCl_2$ and NaCl solutions [23,24]. However, the corrosive effect of the NaCl solution is significantly more severe than that of the $MgCl_2$ solution. In the former case, pitting sites remain relatively dispersed with shallower pit depths, and the contour of the metallic substrate remains discernible even after 28 days of exposure. In contrast, under NaCl conditions, the pits exhibit a high density, large size, and clustered distribution from the early stage, and corrosion severity increases with prolonged exposure. The pit depth increases markedly, accompanied by a substantial expansion of the light-yellow corrosion product layer surrounding the pits, ultimately leading to complete destruction of the original substrate morphology and severe pitting corrosion on the specimen surface [25,26].

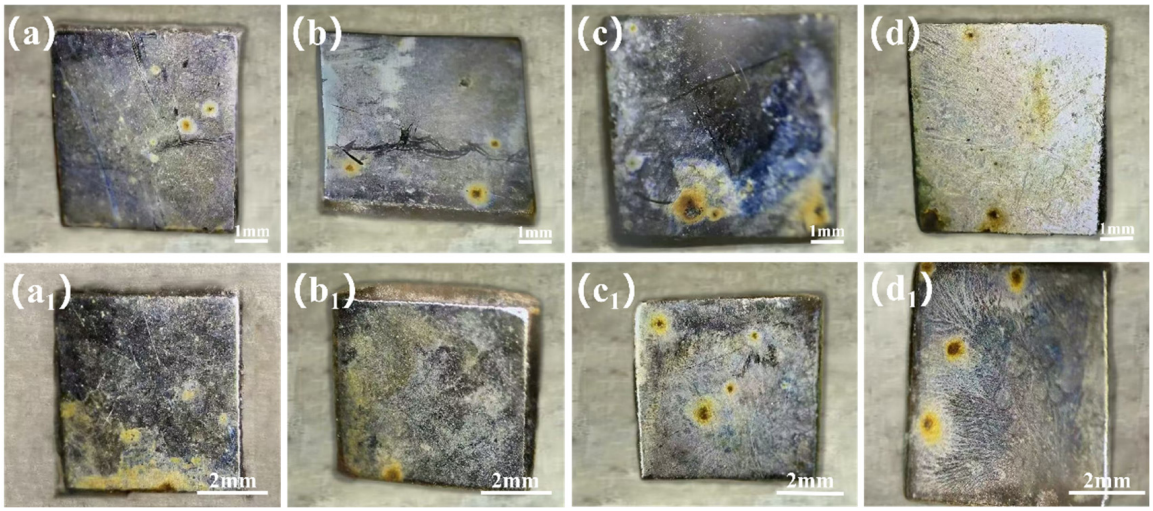

Figure 2. Macroscopic surface morphologies after corrosion in $MgCl_2$ and NaCl solutions: (**a**–**d**) $MgCl_2$ for 7, 14, 21, and 28 days; (**a_1**–**d_1**) NaCl for 7,14, 21, and 28 days.

3.2. Morphological Analysis of Corrosion Products

The microstructural characteristics of the high-entropy alloy specimens used in this study are shown in Figure 3. After hot isostatic pressing, the alloy exhibits a uniform and dense single-phase solid-solution microstructure, without observable second-phase precipitation, elemental segregation, or grain boundary cracking. The grains are approximately equiaxed with a relatively narrow size distribution and strong intergranular cohesion. Only a small number of micropores with sizes below 1 μm are locally observed at grain boundaries, which are unavoidable minor defects formed during fabrication and are expected to have a negligible influence on the overall mechanical properties and corrosion behavior. Elemental mapping further confirms that the principal elements-Cr, Mn, Fe, Co, and Ni-are homogeneously distributed throughout the alloy, with no evident enrichment or depletion, indicating the formation of a thermodynamically stable solid-solution structure. However, despite this compositional uniformity, Mn has a relatively lower standard electrode potential compared to other constituent elements and is therefore more susceptible to preferential dissolution during corrosion [27], particularly in chloride-containing environments. This

selective dissolution may locally modify the composition and chemistry of the passive film, thereby affecting its stability and protective properties. Therefore, although the alloy initially exhibits excellent compositional uniformity and structural integrity, the potential preferential dissolution of Mn should be taken into account when interpreting its corrosion behavior and passivation mechanisms in $MgCl_2$ and NaCl media. Overall, the uniform microstructure provides a reliable baseline for systematically investigating these effects.

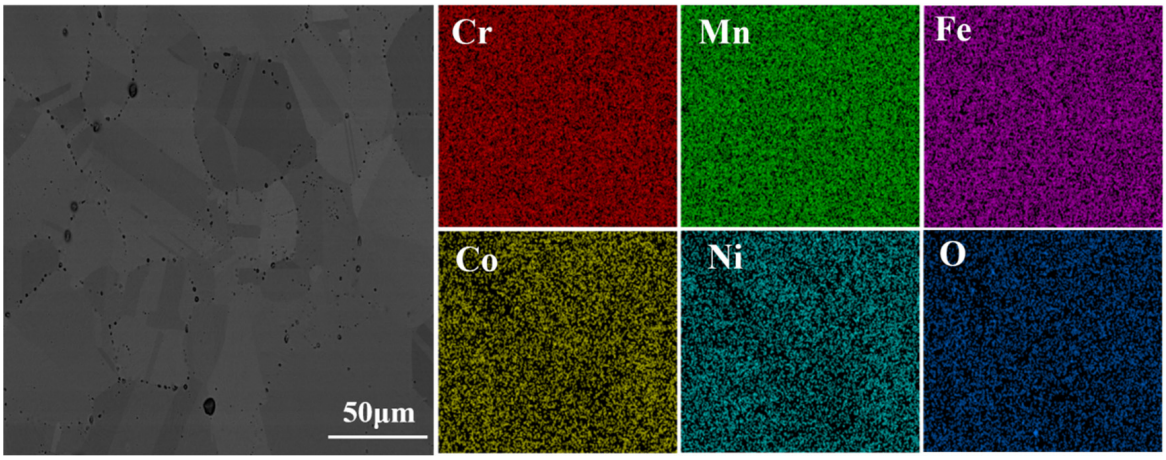

Figure 3. Microstructural images of CrMnFeCoNi HEA and their corresponding EDS spectra.

From the macroscopic corrosion morphologies of the specimens (Figure 4), distinct corrosion pits were observed on the specimen surfaces under both $MgCl_2$ and NaCl deposition conditions, with a noticeably higher density of pits on the samples exposed to NaCl [28–30]. Notably, yellow patches with a color distinctly different from that of the substrate were observed around the edges of the corrosion pits. These features exhibit a concentric ring–like distribution, and their area gradually increases with prolonged corrosion time. Combined with the SEM characterization results, in Figure 4a–d correspond to the surface morphologies of the high-entropy alloy after corrosion in $MgCl_2$ solution for 7, 14, 21, and 28 days, respectively. After 7 days of corrosion (Figure 4a), a small number of corrosion product particles were sparsely distributed on the specimen surface, and no obvious corrosion pits were observed, indicating that the corrosion reaction was relatively mild at the initial stage and that the substrate integrity remained largely intact. After 14 days of corrosion (Figure 4b), the amount of surface corrosion product particles decreased and the surface became relatively smooth. This suggests that partial dissolution or detachment of corrosion products occurred at this stage, and the corrosion process entered a dynamic equilibrium between passive film dissolution and re-passivation, resulting in a decelerated corrosion rate. After 21 days of corrosion (Figure 4c), a limited number of corrosion pits with discernible sizes appeared on the specimen surface, indicating intensified medium attack and localized damage to the substrate, with corrosion penetrating from the surface into the interior. After 28 days of corrosion (Figure 4d), both the number and size of corrosion pits increased markedly. A large amount of fine corrosion products accumulated around the pits, and some pits exhibited deep corrosion characteristics. These observations indicate that corrosion had entered an accelerated stage, with continuous expansion of substrate damage, ultimately leading to the formation of dense and relatively deep corrosion pits. The overall corrosion severity at this stage was significantly higher than that observed at earlier exposure times.

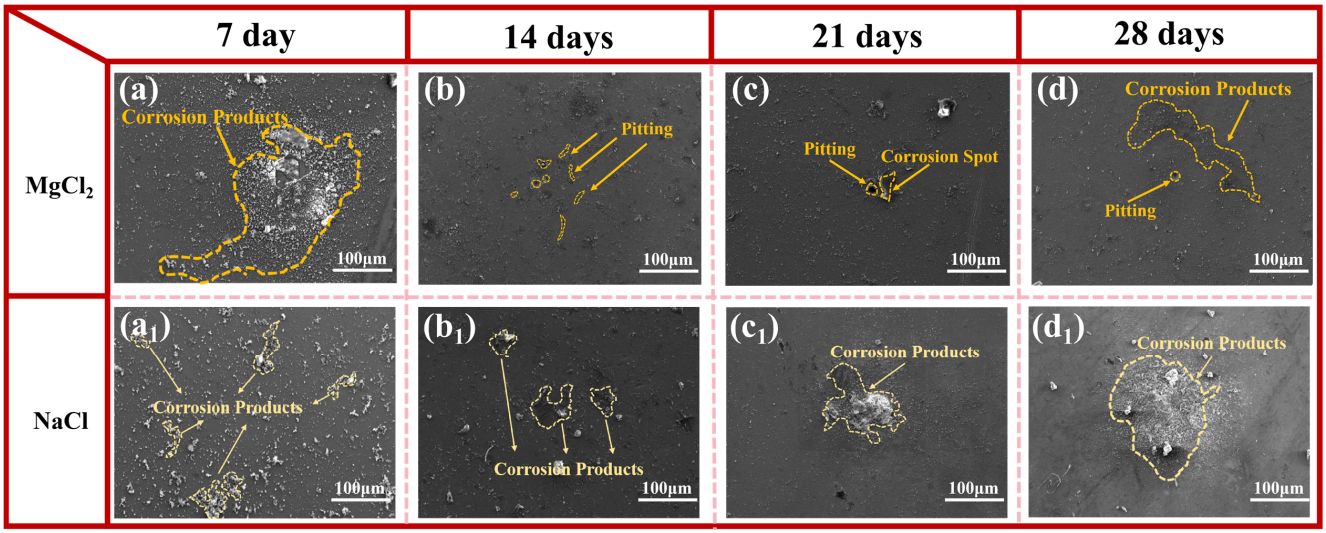

Figure 4. SEM images of the corroded surfaces of the HEAs after exposure to $MgCl_2$ and NaCl solutions under cyclic wet–dry conditions; (**a**–**d**) $MgCl_2$ solution after 7, 14, 21, and 28 days, respectively; (**a$_1$**–**d$_1$**) NaCl solution after 7, 14, 21, and 28 days, respectively.

As shown in Figure 5, after 21 and 28 days of wet–dry cyclic corrosion, distinct cracks appeared within the yellow patches on the specimen surface; however, these features did not spall off and remained locally aggregated during the later stages of corrosion. EDS analysis revealed relatively high contents of O, Cl, and Mg in these regions, suggesting that the yellow patches are likely composite products consisting of Mg^{2+} and Cl^{-} containing salts or metal oxides formed in the $MgCl_2$ environment. Compared with the pitting morphology of 304 stainless steel [31], the high-entropy alloy in this study exhibits more pronounced localized corrosion features. The pits observed in the present work are generally deeper and show clear propagation into the substrate, often accompanied by the accumulation of corrosion products around the pit edges. In contrast, 304 stainless steels typically present relatively shallow and uniformly distributed pits, indicating a more stable passive film and limited pit growth. The observed differences suggest that although both materials undergo pitting corrosion in chloride-containing environments, the high-entropy alloy is more susceptible to pit propagation once the passive film is locally broken down. This phenomenon is particularly pronounced under $MgCl_2$ corrosion conditions, indicating that the presence of Cl^{-} and Mg^{2+} promotes the precipitation and deposition of soluble salts during localized corrosion, thereby leading to the formation of yellow patches around the corrosion pits. In contrast, the high-entropy alloy specimens corroded in NaCl solution exhibited a significantly higher density of pitting sites with deeper pit morphologies, and localized exposure of the substrate was observed in some areas. The corrosion products inside and around the pits were loosely distributed with a rough morphology, and the overall surface integrity was relatively poor. Based on SEM observations, the pit size is estimated to be on the order of several micrometers, with some pits showing clear inward propagation into the substrate, indicating localized corrosion development.

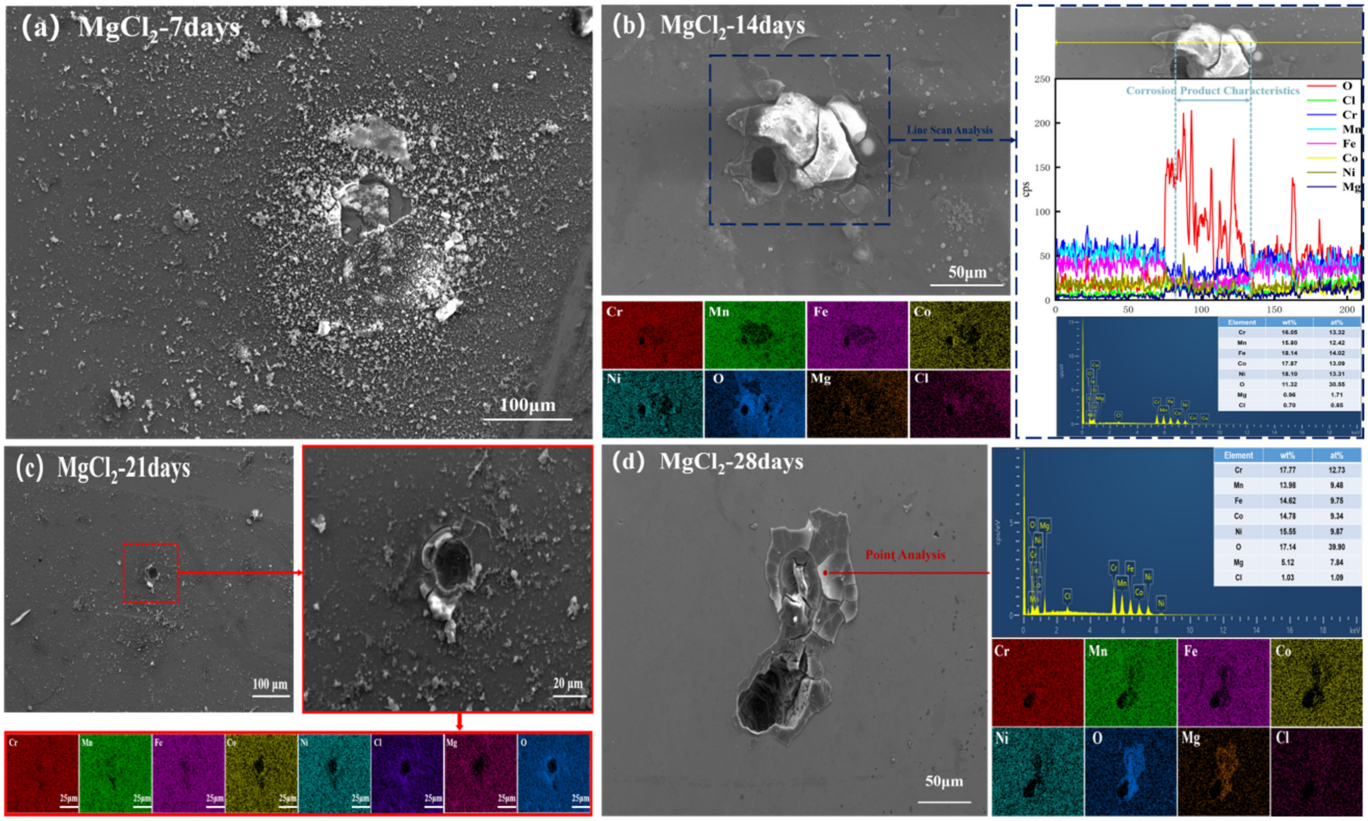

Figure 5. SEM images and EDS analysis of corrosion products on the HEA in $MgCl_2$ solution under cyclic wet–dry conditions: (**a**) 7 days, showing initial pit formation; (**b**) 14 days, including selected region for line scan analysis with corresponding elemental distribution maps; (**c**) 21 days, showing a typical corrosion pit and its magnified view with elemental mapping; (**d**) 28 days, including point analysis with EDS spectrum and quantitative composition.

3.3. Compositional Analysis of Corrosion Products

By combining the SEM observations with the qualitative EDS analysis, the morphological characteristics and chemical composition of the corrosion-affected regions on the high-entropy alloy in chloride-containing environments can be systematically elucidated. SEM results reveal that the corrosion patches on the alloy surface exhibit a heterogeneous, porous, and loosely packed morphology, with pronounced cracking and local spallation in certain areas. Such morphological features directly reflect the aggressive attack of the corrosive medium on the alloy substrate and the inherent instability of the corrosion product layer. Qualitative EDS analysis of the corrosion-affected regions indicates that the corrosion products are primarily composed of oxygen (O), chlorine (Cl), and magnesium (Mg), together with metallic elements originating from the alloy substrate, such as chromium (Cr), iron (Fe), and nickel (Ni). No signals from extraneous impurity elements were detected. Among these elements, oxygen and chlorine are significantly enriched in the corrosion-affected regions, and their coexistence directly confirms the synergistic interaction between oxidation reactions and chloride-induced attack. Oxygen primarily participates in the formation of metal oxides and metal hydroxides (such as Cr-containing corrosion products, Fe-rich corrosion species, and Ni-containing compounds), whereas chlorine readily combines with metal cations from the substrate to form multicomponent metal hydroxy chlorides. The presence of magnesium is closely associated with the $MgCl_2$-containing corrosive medium. It should be noted that the identification of corrosion products based on EDS analysis is qualitative, and it is not sufficient to distinguish between hydroxides, oxides, and hydroxy-chlorides. Therefore, the corrosion products described in this study

are referred to in a general sense based on elemental composition. Mg^{2+} ions participate in the formation of corrosion products in the affected regions through ionic migration in solution, further demonstrating the regulatory role of the corrosive environment on the composition of the corrosion products. Metallic elements such as Cr, Fe, and Ni originate from the selective dissolution of the high-entropy alloy substrate and subsequent surface redeposition. During the corrosion process, metal atoms within the substrate lose electrons to form metal cations, a portion of which migrate toward the surface and react with anions in the solution, including O^{2-}, OH^-, and Cl^-, ultimately depositing in the corrosion-affected regions and constituting the principal metallic components of the composite corrosion products. Based on the combined morphological observations and compositional analyses, it can be concluded that the corrosion patches formed on the high-entropy alloy in chloride-containing environments are not composed of a single phase. Instead, they consist of a multicomponent composite system comprising metal oxides, metal hydroxides, and metal hydroxy chlorides. This compositional complexity is closely correlated with the porous and loosely packed morphology of the corrosion patches and provides direct experimental evidence for elucidating the corrosion behavior and mechanisms of high-entropy alloys in chloride environments.

3.4. Electrochemical Impedance Behavior

To investigate the corrosion kinetics and the evolution of interfacial characteristics of the high-entropy alloy after exposure to $MgCl_2$ or NaCl solutions, EIS was employed to evaluate the interfacial responses at different corrosion durations (0, 7, 14, 21, and 28 days). The obtained EIS data were fitted using ZsimpWin software. This analysis elucidates the formation, dissolution, and breakdown mechanisms of the surface passive film during the corrosion process, providing a theoretical basis for optimizing the corrosion resistance of high-entropy alloys in chloride-containing environments. As shown in Figure 6, panels a,b and a_1,b_1 present the Nyquist plots, Bode plots, and their evolution with exposure time for the high-entropy alloy in 0.2 mol/L $MgCl_2$ solution and 0.4 mol/L NaCl solution, respectively. Simultaneously, the simplified equivalent circuit models (Figure 6c,c_1) were employed to fit the impedance data, facilitating a more intuitive interpretation of the impedance variation trends. The elements used in the equivalent circuit are defined as follows: Rs represents the solution resistance, R_r and R_{ct} denote the resistances of the corrosion product layer and the charge transfer process, respectively, while Q_r and Q_{dl} correspond to the protective layer capacitance and the double-layer capacitance. The fitted EIS parameters for the high-entropy alloy in 0.2 mol/L $MgCl_2$ and 0.4 mol/L NaCl solutions are listed in Table 3. It is noteworthy that, although some studies calculate corrosion rates based on the polarization resistance (R_p), in the present study, the charge transfer resistance (R_{ct}) is considered more directly correlated with the corrosion rate, as R_{ct} exclusively reflects the Faradaic process controlled by charge transfer. Therefore, the reciprocal of R_{ct} ($1/R_{ct}$) is used here as a parameter representing the corrosion rate of the high-entropy alloy under simulated salt-lake atmospheric conditions (Figure 6d,d_1).

The results indicate that the Nyquist plots of the samples subjected to $MgCl_2$ corrosion for different durations (0, 7, 14, 21, and 28 days) all exhibit typical single capacitive semicircles, with no evident diffusion-controlled arcs, suggesting that the corrosion process is primarily governed by charge transfer. For the uncorroded sample, the impedance semicircle is relatively small and narrow, corresponding to a low total resistance ($R_{ct} + R_r$), which can be attributed to the limited thickness and intact structure of the native passive film on the alloy surface. This indicates that the initial corrosion resistance of the alloy is at a moderate level.

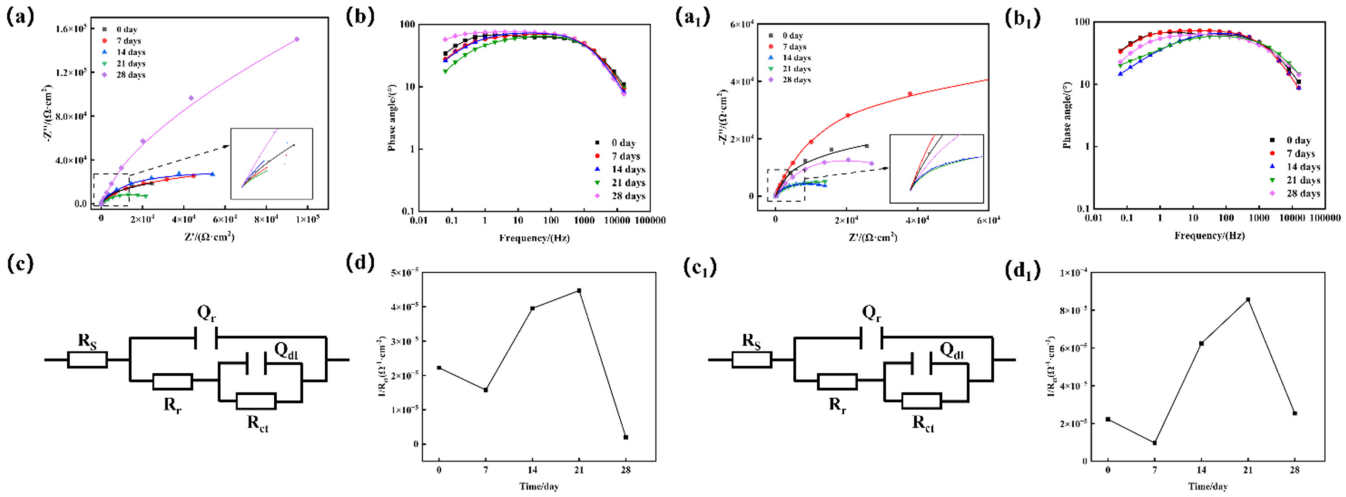

Figure 6. Electrochemical responses of high-entropy alloys during corrosion in $MgCl_2$ and NaCl solutions: (**a**,**b**) Nyquist and Bode plots in $MgCl_2$ solution; (**a$_1$**,**b$_1$**) Nyquist and Bode plots in NaCl solution; (**c**,**c$_1$**) equivalent circuit models used for EIS fitting; (**d**) reciprocal of Rct in $MgCl_2$ solution; (**d$_1$**) reciprocal of Rct in NaCl solution.

Table 3. Fitting results of EIS parameters.

$MgCl_2$ Corrosion	R_s ($\Omega \cdot cm^2$)	Q_r y_r ($\Omega^{-1} \cdot cm^{-2} \cdot S^{-n}$)	n_r	R_r ($\Omega \cdot cm^2$)	Q_{dl} y_{dl} ($\Omega^{-1} \cdot cm^{-2} \cdot S^{-n}$)	n_{dl}	R_{ct} ($\Omega \cdot cm^2$)
0 day	15.27	3.60×10^{-5}	0.78	2764	1.10×10^{-5}	1	44,988
7 days	27.19	1.33×10^{-5}	0.83	9039	1.09×10^{-5}	0.61	63,455
14 days	31.41	1.25×10^{-5}	0.84	52,925	4.97×10^{-5}	0.98	25,285
21 days	31.29	1.62×10^{-5}	0.80	6673	2.49×10^{-5}	0.68	22,360
28 days	33.88	1.08×10^{-5}	0.86	20,400	2.64×10^{-5}	0.83	495,950
NaCl Corrosion	**R_s ($\Omega \cdot cm^2$)**	**Q_r y_r ($\Omega^{-1} \cdot cm^{-2} \cdot S^{-n}$)**	**n_r**	**R_r ($\Omega \cdot cm^2$)**	**Q_{dl} y_{dl} ($\Omega^{-1} \cdot cm^{-2} \cdot S^{-n}$)**	**n_{dl}**	**R_{ct} ($\Omega \cdot cm^2$)**
0 day	15.27	3.57×10^{-5}	0.78	2764	5.26×10^{-5}	1	44,988
7 days	25.12	1.46×10^{-5}	0.81	60.6	2.10×10^{-6}	0.90	103,100
14 days	34.27	1.27×10^{-5}	0.83	4531	5.70×10^{-5}	0.63	16,013
21 days	31.35	2.38×10^{-5}	0.72	10,375	1.51×10^{-4}	0.68	11,676
28 days	29.49	2.74×10^{-5}	0.71	305.1	1.20×10^{-6}	0.91	39,398

After 7~14 days of simulated salt-lake atmospheric corrosion under cyclic wet–dry conditions, the radius of the impedance semicircle significantly increased. By day 7, the alloy elements reacted with the corrosive medium to form corrosion products, primarily Cr_2O_3-based oxides and hydroxides, which gradually deposited to form an initial product layer. Although this layer was not fully dense, it effectively reduced the charge transfer rate, leading to an increase in the overall system impedance. By day 14, the corrosion product layer had further thickened and densified. In addition, the "cocktail effect" of the high-entropy alloy facilitated the cooperative interaction of different elemental components to fill defects within the film, substantially enhancing its integrity and stability.

By day 21 of corrosion, the impedance semicircle markedly contracted, indicating a "failure transition" of the corrosion product layer. During prolonged corrosion, localized attack by Cl^- ions induced cracking and spallation of the product film, allowing the corrosive medium to directly contact the alloy substrate, which resulted in a sharp decrease in the charge transfer resistance (R_{ct}). By day 28, the impedance at the high-frequency region of the Nyquist plots suddenly increased. This is attributed to the formation of a high-resistance composite layer on the alloy surface, consisting of Mg-containing complex salt corrosion products and residual passive film, which substantially suppressed the charge transfer process and elevated the system impedance by an order of magnitude.

In contrast, for corrosion in NaCl solution, the radius of the impedance semicircle reached its maximum on day 7 and subsequently decreased continuously. This trend indicates that the corrosion kinetics of the high-entropy alloy exhibit distinct stage-dependent behavior in the two different corrosive media. The Bode plots (Figure 6b,b_1) further reveal that the phase angle of the sample in $MgCl_2$ solution maintained a single-peak feature throughout the entire corrosion period, whereas in NaCl solution, a double-peak feature appeared in the phase angle after 28 days of exposure. This difference arises from the more uniform structure of the corrosion product layer formed in $MgCl_2$, whereas in NaCl, localized corrosion occurs during the later stages, resulting in a "dual-interface" structure comprising both the product layer and the underlying substrate.

The fitted electrochemical parameters indicate that the reciprocal of R_{ct} can be used to represent the corrosion rate of the high-entropy alloy under simulated salt-lake atmospheric conditions; thus, a higher R_{ct} value corresponds to a lower corrosion rate. In the $MgCl_2$ medium, the charge transfer resistance (R_{ct}) reached a local maximum at day 7 during the early stage of corrosion and then gradually decreased from days 14 to 21, indicating that the corrosion rate initially slowed and subsequently accelerated. This variation is closely related to the staged processes of passive film breakdown, formation of the corrosion product layer, and eventual failure of the film in the later stages [32–34]. By day 28, the R_{ct} value in $MgCl_2$ solution increased sharply, which is attributed to the formation of a high-resistance composite layer that suppressed the corrosion process. The variation trend of R_{ct} in NaCl solution was generally similar to that in $MgCl_2$; however, localized corrosion in the later stages was more severe. In summary, the corrosion process of the high-entropy alloy in $MgCl_2$ can be divided into three stages: passive film formation, film stabilization, and localized pitting. Although the corrosion stages are generally similar in the two chloride media, the corrosive effect of NaCl on the alloy is significantly stronger than that of $MgCl_2$.

4. Discussion

4.1. Formation Mechanism of Yellow Deposits

In both the $MgCl_2$ and NaCl corrosion systems, the yellow deposits formed around the corrosion pits on the surface of the high-entropy alloy are the result of the combined effects of ion migration, interfacial chemical reactions, and local environmental control during the corrosion process. The formation mechanism of these deposits can be comprehensively explained from two aspects: corrosion product deposition and transformation, and the evolution of the local microenvironment. From the perspective of corrosion product deposition and transformation, during the early stage of corrosion in chloride-containing solutions, the high-entropy alloy spontaneously forms a dense passive film, with Cr_2O_3 as the core. Chloride ions (Cl^-) in the solution adsorb at defect sites such as grain boundaries and dislocations, creating active dissolution zones. At this stage, the alloy's main metal components, such as Fe and Cr, undergo anodic dissolution, releasing metal cations like Fe^{2+} and Cr^{3+}. Meanwhile, dissolved oxygen in the solution is reduced at the cathodic sites, generating a large quantity of hydroxide ions (OH^-). The dissolved metal cations then react with OH^- ions, forming amorphous metal hydroxide chloride precursors. These precursors have very low solubility and rapidly adsorb onto the edges of the corrosion pits due to the concentration gradient, completing the initial deposition. As the corrosion reaction continues, the amorphous precursors undergo dehydration, crystallization, and phase transformation. For example, the brownish-yellow corrosion products are likely associated with iron oxyhydroxides (FeOOH-type species), which commonly form in chloride-containing environments during atmospheric corrosion. These crystalline products form the yellow characteristic and material framework of the yellow deposits observed at the edges of the

corrosion pits [35–37]. From the perspective of the evolution of the local microenvironment, the concave structure of the corrosion pits creates a closed-to-semi-closed local microzone. Due to the poor fluidity of the solution inside the pit, the metal cations accumulate, leading to a concentration several times higher than that in the surrounding corrosive solution. These cations undergo hydrolysis reactions, generating a large amount of H^+ ions, which causes the pH inside the pit to become slightly acidic, while the pit edges exhibit a slightly alkaline environment. This pH gradient drives the migration of metal cations toward the edges of the pit, promoting the preferential deposition of corrosion products around the corrosion pit. Furthermore, chloride ions (Cl^-) continuously adsorb onto the surface, disrupting the passive film while simultaneously forming soluble complexes with the metal cations, promoting ion dissolution. Meanwhile, the unreacted chloride ions accumulate at the interface of the yellow deposit, stabilizing the charge of the corrosion product and inhibiting re-dissolution. This process forms a cyclic "film disruption–ion dissolution–chloride adsorption" loop, providing a continuous supply of material for the growth of the yellow deposit.

4.2. Mechanism Analysis of Corrosion Behavior Differences in $MgCl_2$ and NaCl Environments

For high-entropy alloys, the corrosion behavior in both $MgCl_2$ and NaCl chloride-containing systems follows a common evolutionary sequence of "passive film formation-chloride-induced film breakdown-localized corrosion propagation", as schematically illustrated in Figure 7. The cross-sectional features shown in the schematic diagram are inferred based on surface observations, electrochemical results, and previously reported studies on similar corrosion systems. At the initial stage of corrosion, a passive film dominated by chromium oxide (Cr_2O_3) spontaneously forms on the alloy surface through oxidation reactions. Owing to its compact crystal structure, this passive layer effectively blocks direct contact between the corrosive medium and the alloy substrate, thereby suppressing anodic dissolution and maintaining the alloy in a quasi-stable corrosion state. However, Cl^- ions in the solution preferentially adsorb and accumulate at defect sites within the passive film, such as dislocations, grain boundaries, and micro-pores. Subsequently, Cl^- ions diffuse into the interior of the passive layer, where they complex with metal cations to form soluble metal–chloride complexes. This complexation process induces localized dissolution of the passive film, generating microscopic breakdown sites. Meanwhile, the continuous ingress of Cl^- ions lead to stress concentration at the passive film/substrate interface, accelerating film cracking and spallation. Once the integrity of the passive film is compromised, the exposed alloy substrate undergoes rapid anodic dissolution, forming corrosion-active sites. Simultaneously, the surrounding intact passive film regions act as cathodes where oxygen reduction reactions occur, establishing anodic-cathodic galvanic couples. This electrochemical coupling ultimately triggers pitting corrosion and promotes its inward propagation into the alloy matrix.

The core mechanism of the Cl^--induced localized corrosion process lies in the formation and evolution of an occluded corrosion cell within the corrosion pit [38–40]. As the corrosion reaction proceeds, dissolved metal cations accumulate within the pit. To maintain charge neutrality, Cl^- ions continuously migrate into the pit, gradually forming an occluded zone that is relatively isolated from the bulk solution. Within this confined region, metal cations undergo hydrolysis reactions, generating a large amount of H^+ and causing a sharp decrease in the local pH. The acidic environment not only suppresses the hydrolysis of Cl^-, allowing it to remain in a free ionic state, but also accelerates the dissolution of the metal substrate inside the pit and inhibits the re-formation of the passive film. Consequently, the highly acidic and Cl^--enriched occluded environment inside the pit contrasts sharply with the relatively neutral, low-Cl^- activity environment outside the

pit, creating pronounced concentration and pH gradients. These gradients constitute a typical occluded corrosion cell, which further amplifies the polarization difference between the anodic and cathodic regions. Specifically, the acidification and high Cl^- activity at the anodic pit interior continuously accelerate metal dissolution, while the newly generated metal cations attract additional Cl^- ions to migrate into the pit. This self-catalytic feedback loop ultimately intensifies localized corrosion and promotes the sustained growth of corrosion pits.

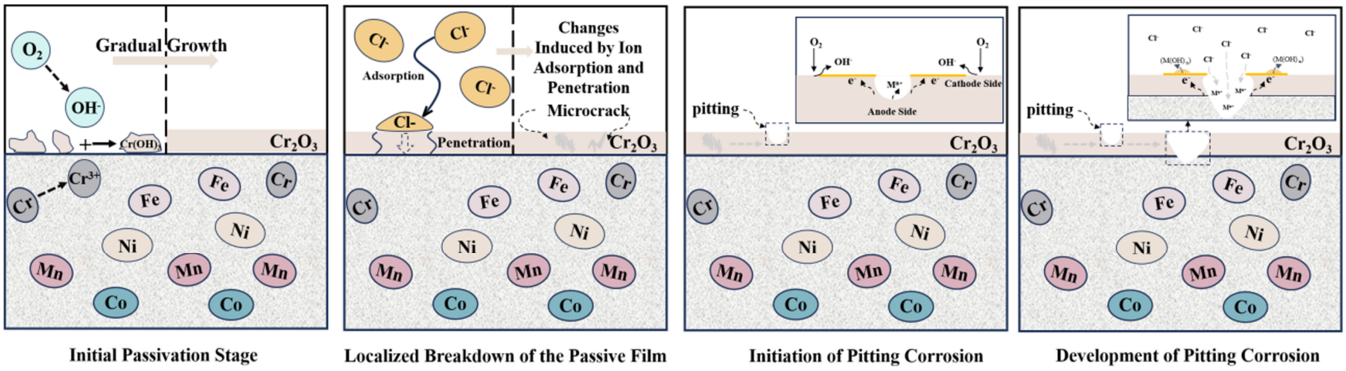

Figure 7. Schematic diagram of the corrosion mechanism.

Although the corrosion of the high-entropy alloy in $MgCl_2$ and NaCl solutions follows the common mechanism described above, differences in ionic characteristics and solution chemistry between the two systems lead to pronounced variations in corrosion severity. In particular, the corrosion degree in NaCl solution is significantly higher than that in $MgCl_2$ solution. The underlying reasons can be mainly attributed to the following two aspects. First, the regulation of solution acidity/alkalinity and Cl^- activity by cations plays a critical role. In $MgCl_2$ solution, Mg^{2+} undergoes hydrolysis, rendering the solution weakly acidic. The hydrolysis product, colloidal $Mg(OH)_2$, can adsorb onto the alloy surface and form a physical barrier, which not only reduces the diffusion rate of Cl^- toward the metal/solution interface but also neutralizes local alkalinity, thereby suppressing the cathodic oxygen reduction reaction. In contrast, Na^+ ions in NaCl solution do not undergo hydrolysis, and the solution remains nearly neutral. Under neutral conditions, Cl^- exhibits higher chemical activity, and in the absence of a $Mg(OH)_2$ colloidal barrier, Cl^- can rapidly adsorb, diffuse, and penetrate the passive film, thereby accelerating its breakdown and promoting anodic dissolution. Second, the effect of cations on the stability of the passive film is also crucial. Mg^{2+} exhibits a relatively strong polarization ability and may interact with oxygen-containing species at the alloy surface or within the corrosion product layer, thereby modifying the interfacial chemistry and passivation behavior. The resulting Mg-containing surface products tend to form a more compact and protective layer, which effectively enhances resistance to Cl^- attack and delays the degradation of the passive layer. By contrast, Na^+ has a much weaker polarization ability and cannot participate in passive film reconstruction, thus providing no stabilizing effect on the passive layer. Consequently, the passive film in NaCl solution deteriorates much faster than that in $MgCl_2$ solution, causing the high-entropy alloy to enter the accelerated corrosion stage at an earlier time.

It is worth noting that although Mg^{2+} and Na^+ are present in the corrosion environments, their direct influence on the corrosion behavior of the high-entropy alloy is relatively limited. The corrosion process is primarily governed by aggressive Cl^- ions, which can penetrate and destabilize the passive film, leading to localized corrosion. Na^+ is generally considered an inert cation and does not actively participate in electrochemical corrosion reactions. In contrast, Mg^{2+} may contribute to the formation of surface deposits such as Mg-containing compounds; however, these products are typically porous and do not pro-

vide effective protection against corrosion. Therefore, the differences in corrosion behavior between $MgCl_2$ and NaCl systems are mainly attributed to environmental factors, such as moisture retention and solution chemistry, rather than the direct effect of Mg^{2+} or Na^+ ions.

4.3. Effect of Cyclic Wet–Dry Alternation on the Corrosion Behavior of High-Entropy Alloys

As a typical corrosive condition used to simulate the high-altitude salt-lake environment, cyclic wet–dry alternation exerts a multidimensional regulatory effect on the pitting corrosion behavior of high-entropy alloys. By altering ion transport processes and the evolution of corrosion products, it significantly influences the initiation and propagation of corrosion. The following discussion elaborates in detail on the mechanistic effects of wet–dry cycling on the surface corrosion behavior of high-entropy alloys. On the one hand, under the corrosion environment regulated by wet–dry alternation, the corrosion kinetics under cyclic wet–dry conditions are strongly influenced by temperature and relative humidity. Higher temperature (40 °C) accelerates electrochemical reactions and enhances ion mobility, thereby promoting corrosion processes. At high relative humidity (80% RH), a continuous electrolyte film can be maintained on the surface, facilitating ionic transport and accelerating corrosion. In contrast, at lower humidity (20% RH), the electrolyte layer becomes discontinuous, limiting electrochemical reactions and slowing down corrosion. During the "wet period", the high-concentration $MgCl_2$ solution is uniformly applied to the specimen surface, enabling sufficient contact with the alloy. Chloride ions (Cl^-) adsorb onto and penetrate the passive film, attacking it and inducing localized breakdown. Upon entering the "dry period", evaporation of the $MgCl_2$ solution leads to the enrichment and concentration of residual Cl^- ions at the sites of passive film rupture, thereby intensifying their destructive effect on the passive layer as the local chloride concentration increases. When the subsequent "wet period" begins, the freshly supplied corrosive solution comes into contact with the passive film that has already been degraded by concentrated Cl^- ions, further accelerating its dissolution. This repeated cycle of "breakdown–concentration–re-breakdown" progressively promotes localized corrosion development [41–43]. This process causes the repair of the passive film to consistently lag behind its degradation, ultimately leading to the extensive nucleation of pitting corrosion sites and creating favorable conditions for the subsequent growth and deepening of corrosion pits. Macroscopically, this manifests as small, visually discernible spots on the alloy surface, around which light-yellow corrosion products can be observed. On the other hand, during the "wet period", metal dissolution releases ions (such as Fe^{2+} and Mn^{2+}), which react with OH^- and Cl^- in the solution to form corrosion products including hydroxides and chlorides. During the "dry period", these products undergo dehydration and crystallization as the solution evaporates, forming a dense corrosion product layer around the corrosion pits and even along the pit walls. From another perspective, this corrosion product layer can temporarily hinder direct contact between the corrosive solution and the substrate, thereby retarding corrosion progression. However, due to the cyclic wet–dry alternation, the product layer tends to locally spall, exposing fresh substrate and creating new corrosion-active sites, which gives rise to an "intermittent burst" characteristic of the corrosion process. For high-entropy alloys, the presence of multiple principal elements results in compositional heterogeneity of the corrosion products (e.g., the coexistence of Cr-rich oxides and Fe-rich chlorides), further intensifying the complexity of the corrosion behavior. In summary, cyclic wet–dry alternation influences the pitting corrosion behavior of high-entropy alloys by reconstructing the balance between "damage and repair" at the corrosion interface, amplifying the autocatalytic effects within corrosion pits, and regulating the evolution of corrosion products, thereby leading to accelerated, more complex, and more heterogeneous corrosion characteristics. In the present study, the introduction of cyclic wet–dry corrosion

testing not only provides a more realistic simulation of the harsh atmospheric conditions of high-altitude salt-lake environments but also reveals the intrinsic corrosion behavior of high-entropy alloys under dynamic wet–dry conditions. These findings offer a more targeted scientific basis for corrosion protection strategies in practical applications involving salt-lake, coastal, and other complex service environments.

5. Conclusions

This study focuses on the corrosion resistance of high-entropy alloys in high-altitude salt-lake environments, systematically investigating their corrosion behavior and underlying mechanisms. The results provide both theoretical support and experimental evidence for the application of high-entropy alloys in engineering scenarios such as salt-lake resource development. Based on analyses conducted using SEM, EDS and electrochemical measurements, the main conclusions can be summarized as follows:

(1) The prepared high-entropy alloy exhibits a homogeneous and dense single-phase solid-solution structure, in which the principal elements Cr, Mn, Fe, Co, and Ni are uniformly distributed without obvious elemental segregation or secondary phase precipitation. The corrosion products consist of a multicomponent composite system composed of metal oxides, metal hydroxides, and metal hydroxychlorides. The protective effectiveness of the corrosion product layer is strongly dependent on its structural compactness: a dense and continuous product film effectively inhibits Cl^- penetration and retards corrosion progression, whereas a loose, porous, or cracked film provides pathways for corrosive media ingress, thereby promoting pitting corrosion.

(2) Electrochemical test results indicate that the corrosion processes of the high-entropy alloy in the two chloride-containing media are generally similar. The R_{ct} value in the $MgCl_2$ system reaches 4.96×10^5 $\Omega \cdot cm^2$ in 28 days, which is significantly higher than that in the NaCl system, indicating a lower corrosion rate. NaCl exhibits a significantly stronger corrosive effect on the alloy compared to $MgCl_2$.

(3) Corrosion mechanism analysis reveals that the corrosion of the high-entropy alloy in salt-lake environments follow a dynamic evolution characterized by "anodic dissolution–product deposition–film failure", which is fundamentally different from the corrosion mechanism of conventional alloys dominated solely by passive film breakdown. This study provides new insights into compositional optimization of high-entropy alloys and the design of corrosion protection strategies for service in salt-lake environments.

Author Contributions: Conceptualization, S.Y. and D.J.; methodology, S.Y., J.L. and J.Z.; software, S.Y., Z.W. and X.L.; validation, S.Y., J.L., S.G. and Z.R.; formal analysis, S.Y., J.L. and H.Z.; investigation, S.Y., J.L., S.G., Z.R. and Y.P.; resources, D.J., L.C., Z.W. and X.L.; data curation, S.Y. and J.L.; writing—original draft preparation, S.Y.; writing—review and editing, D.J., J.Z., H.Z., Y.P. and L.C.; visualization, S.Y. and J.L.; supervision, D.J.; project administration, D.J.; funding acquisition, D.J. All authors have read and agreed to the published version of the manuscript.

Funding: This research received no external funding.

Data Availability Statement: The original contributions presented in this study are included in the article. Further inquiries can be directed to the corresponding author.

Conflicts of Interest: Authors Lida Che, Zhanfang Wu and Xiangyang Li were employed by the CISRI HIPEX Technology Co., Ltd. The remaining author declare that the research was conducted in the absence of any commercial or financial relationships that could be construed as a potential conflict of interest.

References

1. Last, W.M. Geolimnology of salt lakes. *Geosci. J.* **2002**, *6*, 347–369. [CrossRef]
2. Zheng, M.; Liu, X. Hydrochemistry of Salt Lakes of the Qinghai-Tibet Plateau, China. *Aquat. Geochem.* **2009**, *15*, 293–320. [CrossRef]
3. Zheng, M.; Zhang, Y.; Liu, X.; Qi, W.; Kong, F.; Nie, Z.; Pu, L.; Hou, X.; Wang, H.; Zhang, Z.; et al. Progress and prospects of salt lake research in China. *Acta Geol. Sin.-Engl. Ed.* **2016**, *90*, 1195–1235. [CrossRef]
4. Li, Q.; Fan, Q.; Wang, J.; Qin, Z.; Zhang, X.; Wei, H.; Du, Y.; Shan, F. Hydrochemistry, distribution and formation of lithium-rich brines in salt lakes on the Qinghai-Tibetan Plateau. *Minerals* **2019**, *9*, 528. [CrossRef]
5. Ren, P.; Yin, Z.; Wang, G.; Zhao, H.; Ji, P. The sustainable supply of lithium resources from the Qinghai-Tibet plateau salt lakes group: The selection of extraction methods and the assessment of adsorbent application prospects. *Desalination* **2024**, *583*, 117659. [CrossRef]
6. Kim, Y.-K.; Joo, Y.-A.; Kim, H.S.; Lee, K.-A. High temperature oxidation behavior of Cr-Mn-Fe-Co-Ni high entropy alloy. *Intermetallics* **2018**, *98*, 45–53. [CrossRef]
7. Ostovari Moghaddam, A.; Sudarikov, M.; Shaburova, N.; Zherebtsov, D.; Zhivulin, V.; Solizoda, I.A.; Starikov, A.; Veselkov, S.; Samoilova, O.; Trofimov, E. High temperature oxidation resistance of W-containing high entropy alloys. *J. Alloys Compd.* **2022**, *897*, 162733. [CrossRef]
8. Zhang, Y.; Zuo, T.T.; Tang, Z.; Gao, M.C.; Dahmen, K.A.; Liaw, P.K.; Lu, Z.P. Microstructures and properties of high-entropy alloys. *Prog. Mater. Sci.* **2014**, *61*, 1–93. [CrossRef]
9. Ye, Y.F.; Wang, Q.; Lu, J.; Liu, C.T.; Yang, Y. High-entropy alloy: Challenges and prospects. *Mater. Today* **2016**, *19*, 349–362. [CrossRef]
10. Miracle, D.B.; Senkov, O.N. A critical review of high entropy alloys and related concepts. *Acta Mater.* **2017**, *122*, 448–511. [CrossRef]
11. Zeng, Y.; Le, Z.; Zhu, M.; Liu, L.; Shen, J.; Zhu, G. Effects of Cl-concentration, temperature and AC interference on metastable pitting behavior of CoCrFeMnNi High-entropy alloy in a simulated concrete pore solution. *Int. J. Electrochem. Sci.* **2022**, *17*, 221181. [CrossRef]
12. Song, L.F.; Hu, W.B.; Liao, B.K.; Wan, S.; Kang, L.; Guo, X.P. Corrosion behavior of $AlCoCrFeNi_{2.1}$ eutectic high-entropy alloy in Cl--containing solution. *J. Alloys Compd.* **2023**, *938*, 168609.
13. Xie, Z.; Liu, B.; Fu, A.; Li, K.; Cao, Y.; Zhou, H.; Peng, J.; Liu, Y. Combating Cl^- and SO_4^{2-}-induced molten salt corrosion by laser cladding FeCrNiMoAl high-entropy alloy coating. *Surf. Coat. Technol.* **2024**, *494*, 131429. [CrossRef]
14. Ye, Q.F.; Feng, K.; Li, Z.G.; Lu, F.G.; Li, R.F.; Huang, J.; Wu, Y.X. Microstructure and corrosion properties of CrMnFeCoNi high entropy alloy coating. *Appl. Surf. Sci.* **2017**, *396*, 1420–1426. [CrossRef]
15. Tang, Z.; Senkov, O.N.; Parish, C.M.; Zhang, C.; Zhang, F.; Santodonato, L.J.; Wang, G.Y.; Zhao, G.F.; Yang, F.Q.; Liaw, P.K. Tensile ductility of an AlCoCrFeNi multi-phase high-entropy alloy through hot isostatic pressing (HIP) and homogenization. *Mater. Sci. Eng. A* **2015**, *647*, 229–240. [CrossRef]
16. Joseph, J.; Hodgson, P.; Jarvis, T.; Wu, X.H.; Stanford, N.; Fabijanic, D.M. Effect of hot isostatic pressing on the microstructure and mechanical properties of additive manufactured $Al_xCoCrFeNi$ high entropy alloys. *Mater. Sci. Eng. A* **2018**, *733*, 59–70. [CrossRef]
17. Guo, M.; Lu, X.; Tang, J.; Pan, C.; Wang, Z. Corrosion Behavior of 316 Stainless Steel Exposed to a Simulated Salt lake Atmospheric Environment under UV Illumination. *Int. J. Electrochem. Sci.* **2021**, *16*, 210457. [CrossRef]
18. Du, R.J.; An, S.; Sun, Y.R.; Wang, D.; Xie, F. Study on the Corrosion Resistance of Zinc-Graphene Oxide Composite Coatings in Marine Environments. *JOM* **2025**, *78*, 3282–3295. [CrossRef]
19. Qian, B.; Hou, B.R.; Zheng, M. The inhibition effect of tannic acid on mild steel corrosion in seawater wet/dry cyclic conditions. *Corros. Sci.* **2013**, *72*, 1–9. [CrossRef]
20. Thee, C.; Hao, L.; Dong, J.H.; Mu, X.; Wei, X.; Li, X.F.; Ke, W. Atmospheric corrosion monitoring of a weathering steel under an electrolyte film in cyclic wet-dry condition. *Corros. Sci.* **2014**, *78*, 130–137. [CrossRef]
21. Yu, J.X.; Wang, H.K.; Yu, Y.; Luo, Z.; Liu, W.D.; Wang, C.M. Corrosion behavior of X65 pipeline steel: Comparison of wet-Dry cycle and full immersion. *Corros. Sci.* **2018**, *133*, 276–287. [CrossRef]
22. Zhang, X.; Yang, S.W.; Zhang, W.H.; Guo, H.; He, X.L. Influence of outer rust layers on corrosion of carbon steel and weathering steel during wet-dry cycles. *Corros. Sci.* **2014**, *82*, 165–172. [CrossRef]
23. Guo, M.; Tang, J.; Gu, T.; Peng, C.; Li, Q.; Pan, C.; Wang, Z. Corrosion Behavior of 316L Stainless Steels Exposed to Salt Lake Atmosphere of Western China for 8 years. *Acta Metall. Sin. (Engl. Lett.)* **2020**, *34*, 555–564. [CrossRef]
24. Guo, M.; Tang, J.; Peng, C.; Li, X.; Wang, C.; Pan, C.; Wang, Z. Effects of salts and its mixing ratio on the corrosion behavior of 316 stainless steel exposed to a simulated salt-lake atmospheric environment. *Mater. Chem. Phys.* **2022**, *276*, 125380. [CrossRef]
25. Pardo, A.; Merino, M.C.; Coy, A.E.; Viejo, F.; Arrabal, R.; Matykina, E. Pitting corrosion behaviour of austenitic stainless steels-combining effects of Mn and Mo additions. *Corros. Sci.* **2008**, *50*, 1796–1806. [CrossRef]

26. Shi, Y.Z.; Yang, B.; Xie, X.; Brechtl, J.; Dahmen, K.A.; Liaw, P.K. Corrosion of $Al_xCoCrFeNi$ high-entropy alloys: Al-content and potential scan-rate dependent pitting behavior. *Corros. Sci.* **2017**, *119*, 33–45. [CrossRef]
27. Bahmani, A.; Moradi, S.; Lotfpour, M.; Jeong, H.T.; Kim, W.J. Effect of grain size on the corrosion resistance of the $Fe_{41}Mn_{25}Ni_{24}Co_8Cr_2$ high entropy alloy. *Corros. Sci.* **2024**, *230*, 111892. [CrossRef]
28. Qiu, Y.; Thomas, S.; Gibson, M.A.; Fraser, H.L.; Birbilis, N. Corrosion of high entropy alloys. *npj Mater. Degrad.* **2017**, *1*, 15. [CrossRef]
29. Shi, Y.Z.; Yang, B.; Liaw, P.K. Corrosion-Resistant High-Entropy Alloys: A Review. *Metals* **2017**, *7*, 43. [CrossRef]
30. Luo, H.; Li, Z.M.; Mingers, A.M.; Raabe, D. Corrosion behavior of an equiatomic CoCrFeMnNi high-entropy alloy compared with 304 stainless steel in sulfuric acid solution. *Corros. Sci.* **2018**, *134*, 131–139. [CrossRef]
31. Guo, M.; Yin, Q.; Liu, M.; Pan, C.; Wang, Z. Corrosion Behavior of 304 Stainless Steel Exposed to a Simulated Salt Lake Atmosphere. *Acta Metall. Sin. (Engl. Lett.)* **2020**, *33*, 857–870. [CrossRef]
32. Chen, Y.; Duval, T.; Hung, U.; Yeh, J.; Shih, H. Microstructure and electrochemical properties of high entropy alloys—A comparison with type-304 stainless steel. *Corros. Sci.* **2005**, *47*, 2257–2279. [CrossRef]
33. Soare, V.; Burada, M.; Constantin, I.; Mitrică, D.; Bădiliţă, V.; Caragea, A.; Târcolea, M. Electrochemical deposition and microstructural characterization of AlCrFeMnNi and AlCrCuFeMnNi high entropy alloy thin films. *Appl. Surf. Sci.* **2015**, *358*, 533–539. [CrossRef]
34. Xu, Z.; Wang, Y.; Gao, X.; Peng, L.; Qiao, Q.; Xiao, J.; Guo, F.; Wang, R.; Yu, J. Electrochemical deposition and corrosion resistance characterization of FeCoNiCr high-entropy alloy coatings. *Coatings* **2023**, *13*, 1167. [CrossRef]
35. Oh, S.J.; Cook, D.; Townsend, H. Characterization of iron oxides commonly formed as corrosion products on steel. *Hyperfine Interact.* **1998**, *112*, 59–66. [CrossRef]
36. Volovitch, P.; Allely, C.; Ogle, K. Understanding corrosion via corrosion product characterization: I. Case study of the role of Mg alloying in Zn-Mg coating on steel. *Corros. Sci.* **2009**, *51*, 1251–1262. [CrossRef]
37. Volovitch, P.; Vu, T.; Allély, C.; Aal, A.A.; Ogle, K. Understanding corrosion via corrosion product characterization: II. Role of alloying elements in improving the corrosion resistance of Zn–Al–Mg coatings on steel. *Corros. Sci.* **2011**, *53*, 2437–2445. [CrossRef]
38. Yamanaka, K.; Shiratori, H.; Mori, M.; Omura, K.; Fujieda, T.; Kuwabara, K.; Chiba, A. Corrosion mechanism of an equimolar AlCoCrFeNi high-entropy alloy additively manufactured by electron beam melting. *npj Mater. Degrad.* **2020**, *4*, 24. [CrossRef]
39. Zhang, M.; Shi, X.; Li, Z.; Xu, H.; Li, G. Corrosion behaviors and mechanism of $CrFeNi_2$ based high-entropy alloys. *Corros. Sci.* **2022**, *207*, 110562. [CrossRef]
40. Feng, L.; Yang, Y.; Zhao, Y.; Ma, K.; Cui, J. Corrosion behaviors and mechanism of $Al_xCrFeMnCu$ high-entropy alloys in a 3.5 wt% NaCl solution. *Corros. Sci.* **2024**, *233*, 112087. [CrossRef]
41. Nishimura, T.; Katayama, H.; Noda, K.; Kodama, T. Effect of Co and Ni on the corrosion behavior of low alloy steels in wet/dry environments. *Corros. Sci.* **2000**, *42*, 1611–1621. [CrossRef]
42. Cheng, C.-Q.; Klinkenberg, L.-I.; Ise, Y.; Zhao, J.; Tada, E.; Nishikata, A. Pitting corrosion of sensitised type 304 stainless steel under wet–dry cycling condition. *Corros. Sci.* **2017**, *118*, 217–226. [CrossRef]
43. Pan, C.; Guo, M.; Wang, Z. Effect of $MgCl_2$ on the corrosion behavior of copper under periodic wet/dry cycle condition. *J. Mater. Eng. Perform.* **2019**, *28*, 2562–2572. [CrossRef]